Phase structure of the massive chiral Gross-Neveu model from the Hartree-Fock approach

Christian Boehmer,[*] Ulf Fritsch,[+] Sebastian Kraus, and Michael Thies[‡]

Institut für Theoretische Physik III, Universität Erlangen-Nürnberg, D-91058 Erlangen, Germany

(Received 29 July 2008; published 26 September 2008)

The phase diagram of the massive chiral Gross-Neveu model (the massive Nambu–Jona-Lasinio model in 1 + 1 dimensions) is constructed. In the large N limit, the Hartree-Fock approach can be used. We find numerically a chiral crystal phase separated from a massive Fermi gas phase by a 1st order transition. Using perturbation theory, we also construct the critical sheet where the homogeneous phase becomes unstable in a 2nd order transition. A tricritical curve is located. The phase diagram is mapped out as a function of fermion mass, chemical potential and temperature, and compared with the one of the discrete chiral Gross-Neveu model. As a by-product, we illustrate the crystal structure of matter at zero temperature for various densities and fermion masses.

DOI: 10.1103/PhysRevD.78.065043 PACS numbers: 11.10.Kk, 11.10.Wx, 11.15.Pg

I. INTRODUCTION

To map out the phase diagram of hot and dense matter has been a major goal of strong interaction physics during the last decades, both experimentally and theoretically. As is often the case, these efforts have been accompanied by studies of drastically simplified, solvable model problems to sharpen the theoretical tools and get guidance for more realistic cases. Among the few known field theories which are both solvable and possess a nontrivial phase structure, fermionic large N models in 1 + 1 dimensions like the 't Hooft model [1] or Gross-Neveu models [2] are perhaps most instructive, as they share a number of properties with quantum chromodynamics (for a pedagogical review, see Ref. [3]). Given that these models have been formulated back in 1974 already, it is surprising that their phase diagrams as a function of temperature, chemical potential and fermion mass have not yet been fully established. As far as we can tell, the reason is not that these phase diagrams were considered to be uninteresting. Rather, this situation reflects a shortcoming of the first round of theoretical investigations during the 1980s and 1990s with methods too crude to expose the full, rich phase structure. As a consequence, there has been renewed interest recently in this topic with results which also have some bearing on low dimensional condensed matter systems, and the original phase diagrams are still in the process of revision right now. For an update on the current state of the art, see Refs. [4,5] and references therein.

In the present paper, we focus on the phase structure of the massive, chiral Gross-Neveu (GN) model at finite temperature and chemical potential. This model is nothing but the 1 + 1 dimensional Nambu–Jona-Lasinio model [6] with N fermion flavors and a bare mass term explicitly breaking the U(1) ⊗ U(1) chiral symmetry. Its Lagrangian reads

$$\mathcal{L} = \bar{\psi}(\mathrm{i}\partial\!\!\!/ - m_0)\psi + \frac{g^2}{2}[(\bar{\psi}\psi)^2 + (\bar{\psi}\mathrm{i}\gamma_5\psi)^2] \quad (1)$$

where flavor indices are suppressed as usual, i.e., $\bar{\psi}\psi = \sum_{k=1}^{N} \bar{\psi}_k\psi_k$ etc. We are only interested in the 't Hooft limit ($N \to \infty$, $Ng^2 = \text{const}$) in which classic no-go theorems can be bypassed and breakdown of continuous symmetries becomes possible in 1 + 1 dimensions. In spite of the fact that semiclassical methods for solving such models have been developed in the 1970s already [2,7], the full phase diagram of the simple field theory with Lagrangian (1) is still largely unknown. Consider first the chiral limit ($m_0 = 0$) of the model. If one constrains the condensates $\langle\bar{\psi}\psi\rangle$, $\langle\bar{\psi}\mathrm{i}\gamma_5\psi\rangle$ to be spatially constant, the resulting phase diagram is identical to the one from the simpler GN model variant with discrete chiral symmetry and scalar-scalar coupling $(\bar{\psi}\psi)^2$ only. One finds two phases in the (μ, T) plane, a massless and a massive Fermi gas, separated by 1st and 2nd order transitions [8]. As soon as one allows for spatially inhomogeneous condensates, the system takes advantage of the Peierls effect [9] and opens a gap at the Fermi surface. This results in a solitonic chiral crystal phase. The first crystalline solution of the Hartree-Fock (HF) problem which was found is the "chiral spiral" with helical order parameter and a strikingly different phase diagram [3,10]. As pointed out in Ref. [11], these results can also be understood readily in terms of bosonization. Very recently however, they have been challenged by a more sophisticated candidate for the complex order parameter in the form of a chirally twisted crystal, using powerful resolvent methods to generate self-consistent solutions in closed analytical form [5,12]. The implications for the phase diagram have not yet been fully worked out but promise an even richer structure of the solitonic crystal phase than previously thought.

Turning to the massive chiral GN model ($m_0 > 0$), we first should like to remind the reader that the bare parameters g^2, m_0 in Eq. (1) together with the UV cutoff $\Lambda/2$ get

[*]christian.boehmer@theorie3.physik.uni-erlangen.de
[+]ulf.fritsch@physik.uni-erlangen.de
[‡]thies@theorie3.physik.uni-erlangen.de

replaced by two physical, renormalization group invariant parameters m and γ in the process of regularization and renormalization [4,13]. Here, m is the physical fermion mass in the vacuum (set equal to 1 without loss of generality throughout this paper) and γ the "confinement parameter" measuring the explicit violation of chiral symmetry,

$$\frac{\pi}{Ng^2} = \gamma + \ln\frac{\Lambda}{m}, \qquad \gamma := \frac{\pi}{Ng^2}\frac{m_0}{m}. \tag{2}$$

The following bits and pieces are known about the phase structure of the massive model. The phase diagram assuming x-independent condensates only [14] is once again indistinguishable from that of the massive discrete chiral GN model, but this is an artefact of the assumption of homogeneity [4]. As far as inhomogeneous condensates are concerned, it is useful to start from the low density, low temperature limit governed by the isolated baryons of the model. Baryons of the massive chiral GN model were first studied near the chiral limit by means of variational techniques [15] and subsequently via the derivative expansion [16]. They turn out to be closely related to the sine-Gordon kink. A recent numerical HF calculation, supplemented by analytical asymptotic expansions, has been able to follow the baryon mass and structure to arbitrary γ [17]. This was actually done in preparation of the present study. Unlike in the discrete chiral GN model, the self-consistent baryon potentials found were not reflectionless, a serious obstacle for a full analytical solution. Aside from individual baryons relevant to the base line at $T = 0$ of the (γ, μ, T) phase diagram, the vicinity of the tricritical point ($\gamma = 0$, $\mu = 0$, $T = e^C/\pi$) has also been explored in some detail [18]. The phase structure was deduced from a microscopic Ginzburg-Landau (GL) approach, based once again on the derivative expansion. In this work, both first and second order critical lines between homogeneous and inhomogeneous phases were identified. As a result, one already starts to see that the GN models with (broken) discrete and continuous chiral symmetry have totally different phase diagrams, as is indeed expected on the basis of universality arguments.

In the present paper, we report on a solution of the HF problem at finite T, μ for a whole range of γ values and construct a first candidate for the full phase diagram of the massive chiral GN model. It is not yet known what impact the more general, chirally twisted soliton crystals of the massless model discovered in Ref. [12] would have on the massive model, and we cannot contribute anything to this question. Our aim here is to extend the calculations of Ref. [18] near the tricritical point to a significant portion of (μ, T, γ) space, so that a 3D plot of the phase diagram can be drawn and compared with the one from the discrete chiral GN model. We think that such an undertaking is worthwhile in the present situation, but should be followed up by efforts to identify alternative chiral crystal structures which might be thermodynamically more stable [12], or by further attempts to arrive at a full analytical solution as in the case of the discrete chiral GN model [4].

The remaining paper is organized as follows. Section II is devoted to the HF calculation at zero temperature. We explain the general numerical procedure (Sec. II A), discuss analytically the low and high density asymptotics (Sec. II B) and present selected numerical results (Sec. II C). Section III contains all the material about finite temperature and the phase diagram. We briefly outline the thermal HF approach to the grand canonical potential (Sec. III A) and recall previous results from GL theory (Sec. III B). In Sec. III C, we describe in detail how we have obtained the perturbative, 2nd order critical sheet. The nonperturbative, 1st order sheet represents the most difficult part of our analysis, since we can only determine it numerically at present. This is presented in Sec. III D along with the final results. In the concluding Sec. IV, we summarize our findings, compare the phase diagram with other related phase diagrams and identify areas where more work is needed.

II. HARTREE-FOCK CALCULATION OF DENSE MATTER AT $T = 0$

A. Setup of the numerical calculations

The HF calculation in the chiral GN model starts from the Dirac Hamiltonian

$$H = \gamma_5 \frac{1}{i}\frac{\partial}{\partial x} + \gamma^0 S(x) + i\gamma^1 P(x) \tag{3}$$

with scalar and pseudoscalar potentials S, P to be determined self-consistently. In Ref. [17], a numerical HF study including the Dirac sea has been used to construct the baryons of this model. For technical reasons, the calculation was done in a finite interval of length L with antiperiodic boundary conditions for the fermions, using a basis of free, massive spinors in discretized momentum space. Now assume that S, P are periodic with spatial period a. We can actually reduce the HF calculation for such a crystal to the one for a single baryon performed in [17]. We enclose the crystal in a box of length $L = Na$ containing N periods and impose again antiperiodic boundary conditions on the fermion single particle wave functions in this large interval,

$$\psi(L) = -\psi(0). \tag{4}$$

According to the Bloch theorem, the eigenspinors of H are of the form

$$\psi(x) = \phi(x)e^{ipx}, \qquad \phi(x + a) = \phi(x). \tag{5}$$

The boundary condition (4) discretizes the Bloch momenta,

$$p_n = \frac{2\pi}{L}\left(n + \frac{1}{2}\right), \qquad (n \in \mathbb{Z}). \tag{6}$$

For a single period, e.g., the interval $[0, a]$, this implies

quasiperiodic boundary conditions,

$$\psi(a) = e^{i\beta_\nu}\psi(0), \tag{7}$$

where the N discrete values of β_ν parametrize the Nth roots of (-1),

$$\beta_\nu = \frac{2\pi}{N}\left(\nu + \frac{1}{2}\right), \qquad \nu = 0, 1, \ldots, N-1. \tag{8}$$

Hence, to get the spectrum of H with a periodic potential, all we have to do is compute the spectrum for a single "baryon" in an interval of length a with quasiperiodic boundary conditions along the lines of Ref. [17], repeat the calculation N times (for all possible values of the phase β_ν) and collect the spectra. This enables us to take over the calculational method literally from Ref. [17]. We also stick to the conditions

$$S(x) = S(-x), \qquad P(x) = -P(-x), \tag{9}$$

reflecting the difference between scalar and pseudoscalar potentials if parity is unbroken. To evaluate the energy density of the crystal at $T = 0$, we once again combine a numerical diagonalization with perturbation theory for states deep down in the Dirac sea. The technical details like vacuum subtraction, double counting correction and renormalization are identical to those given in Ref. [17] and need not be repeated here.

A key element of the HF approach is self-consistency of the potentials S, P. As explained in Ref. [17], this can be achieved by minimizing the HF energy at a fixed fermion number with respect to the potentials, provided one varies the potentials without any bias. In the present work, we assume periodicity, expand S and P into Fourier series,

$$S(x) = \sum_\ell S_\ell e^{i2\pi\ell x/a}, \qquad P(x) = i\sum_\ell P_\ell e^{i2\pi\ell x/a}, \tag{10}$$

and minimize the HF energy with respect to the Fourier coefficients S_ℓ, P_ℓ, and the spatial period a, using a standard conjugate gradient algorithm. The only other bias put in aside from periodicity are the symmetry relations (9). If the true self-consistent potential $\Delta = S - iP$ would not be strictly periodic but carry a chiral twist,

$$\Delta(x + a) = e^{2i\varphi}\Delta(x), \tag{11}$$

as proposed in a recent study of the massless chiral GN model [5,12], our calculation might still be useful as a variational calculation, but we could miss the true self-consistent potential. Note however that there is so far no claim of nonperiodic potentials in the massive model considered in the present work.

B. Low and high density limits

In the limits of low and high fermion density, the ground state energy can be calculated analytically. If the valence band is completely filled (as is indeed found in the full HF calculation), the spatially averaged baryon density per flavor is related to the period a via

$$\rho = \frac{1}{a} = \frac{p_f}{\pi}. \tag{12}$$

The last equation defines the Fermi momentum p_f. At very low density, we expect the energy density to be determined by the baryon mass,

$$\mathcal{E}_{\rm HF} - \mathcal{E}_{\rm vac} \approx M_{\rm B}\rho. \tag{13}$$

The baryon mass is known already from Ref. [17]. At high density on the other hand, we can use perturbation theory to predict the asymptotic behavior of the energy density. This is a simple generalization of a similar calculation done in Ref. [19] for the massive GN model with broken discrete chiral symmetry; cf. Eqs. (67)–(74) of that paper. It is sufficient to keep the Fourier amplitudes S_0, S_1 and P_1 for this purpose. Standard 2nd order perturbation theory then yields the single particle energies

$$E_{\eta,p} = \eta\,\mathrm{sgn}(p)\left(p + \frac{S_0^2}{2p} + \frac{(S_1 + fP_1)^2}{2(p + p_f)} + \frac{(S_1 - fP_1)^2}{2(p - p_f)}\right) \tag{14}$$

where $\eta = \pm 1$ and

$$f = 1 - 2\delta_{\eta,\mathrm{sgn}(p)}. \tag{15}$$

Along the lines of Ref. [19], we find for the perturbative ground state energy

$$\mathcal{E}_{\rm HF} = -\frac{\Lambda^2}{8\pi} + \frac{p_f^2}{2\pi} + \frac{S_0^2}{2\pi}[\gamma + \ln(2p_f)] - \frac{\gamma S_0}{\pi} + \frac{y^2}{4\pi}[2\gamma - 1 + \ln(y^2)] + \frac{2X^2}{\pi}[\gamma + \ln(4p_f)] \tag{16}$$

where we have set

$$S_1 = X + y/2, \qquad P_1 = X - y/2. \tag{17}$$

Minimizing $\mathcal{E}_{\rm HF}$ with respect to S_0, X and y yields

$$X = 0, \qquad S_0 = \frac{\gamma}{\gamma + \ln(2p_f)} \tag{18}$$

and the equation

$$y[2\gamma + \ln(y^2)] = 0 \tag{19}$$

with the solutions $y = 0$ (homogeneous condensate) and

$$y = \pm e^{-\gamma}. \tag{20}$$

The self-consistent potential $\Delta = S - iP$ for the nontrivial solution $y = e^{-\gamma}$ is inhomogeneous,

$$\Delta(x) = \frac{\gamma}{\gamma + \ln(2p_f)} + \exp\{-2ip_f x - \gamma\}. \tag{21}$$

(The other sign of y merely corresponds to a translation of the crystal by $a/2$.) The ground state energy (16) at the minimum is indeed lower than the one of the homogeneous solution,

$$\mathcal{E}_{\mathrm{HF}}(y \neq 0) - \mathcal{E}_{\mathrm{HF}}(y = 0) = -\frac{1}{4\pi} e^{-2\gamma}. \quad (22)$$

At $\gamma = 0$ this agrees with the result for the chiral spiral [10]. Finally we write down the ground state energy for large p_f, relative to the vacuum. It has the asymptotic behavior

$$\mathcal{E}_{\mathrm{HF}} - \mathcal{E}_{\mathrm{vac}} \approx \frac{p_f^2}{2\pi} - \frac{\gamma^2}{2\pi(\gamma + \ln 2 p_f)} + \frac{1}{4\pi}(1 + 2\gamma - e^{-2\gamma}). \quad (23)$$

Equations (13) for $p_f \to 0$ and (23) for $p_f \to \infty$ are the main results of this section, ready to be compared to full numerical results below.

C. Numerical results

We vary with respect to the Fourier components S_ℓ, P_ℓ which, owing to Eqs. (9) and (10), are real and satisfy $S_{-\ell} = S_\ell$, $P_{-\ell} = -P_\ell$. The actual calculations were done as follows. We use $N = L/a = 8$, i.e., perform single baryon computations with 8 different boundary conditions. In the sum over single particle energies we now have to subtract numbers of O(100 000), as compared to O(10 000) for a single baryon. To keep computations feasible with MAPLE, we had to compromise on the size of the momentum space basis and choose the smallest size which gave sufficient precision in the tests, $\bar{N} = 50$ (corresponding to 201×201 matrices). The total number of single particle states computed by diagonalization is therefore $8 \times 201 = 1608$. We kept all Fourier modes of S, P up to $\ell_{\max} = 6$, so that 14 real parameters had to be varied in total (the period a, S_0, and $\{S_\ell, P_\ell\}$ for $\ell = 1 \ldots 6$). To test our MAPLE code, we computed the energy density of crystals where the analytic solution is known (chiral spiral, massless and massive GN models). In all of these cases the energy density was reproduced correctly to 7 significant digits. The other uncertainty comes from the minimization procedure. It was found that after only 20 conjugate gradient steps, the results as shown in the figures below did not change anymore significantly. Under these conditions, all calculations could still be done using MAPLE on high-end PC's, without need to switch to compiled programming languages.

We now turn to the results of the $T = 0$ computations. Just as in the discrete chiral GN model, we found that it is always energetically advantageous to let the Fermi surface coincide with the lower end of an energy gap, as expected from the Peierls effect. We first illustrate the self-consistent potentials which show no surprise. At low density, one recognizes the shapes of clearly resolved individual baryons from Ref. [17]; see Figs. 1 and 2. At high density where the baryons overlap significantly, the lowest Fourier modes (S_0, S_1, P_1) dominate, as anticipated in our perturbative calculation (Figs. 3 and 4). Increasing γ tends to wash out the oscillations at all densities. The energy difference between the crystal and the homogeneous phase is shown in Fig. 5 for 3 values of γ. As expected, the crystal phase is favored at all densities and γ parameters. The horizontal lines at large p_f show the asymptotic prediction of Eq. (22), whereas the slopes of the straight lines near $p_f = 0$ have been obtained from the baryon masses [17] and the mixed phase of the homogeneous calculation (see the appendix of [19]). This provides us with yet another useful test of the computations. Figure 6 shows the p_f-dependence of the energy density, now relative to the vacuum, for the same three values of γ. The dots are numerical results. The curves have simply been obtained by matching the asymptotic expansions Eqs. (13) and (23), at the point where they coincide (indicated by the cross). At the scale of the figure, the agreement is perfect, reminis-

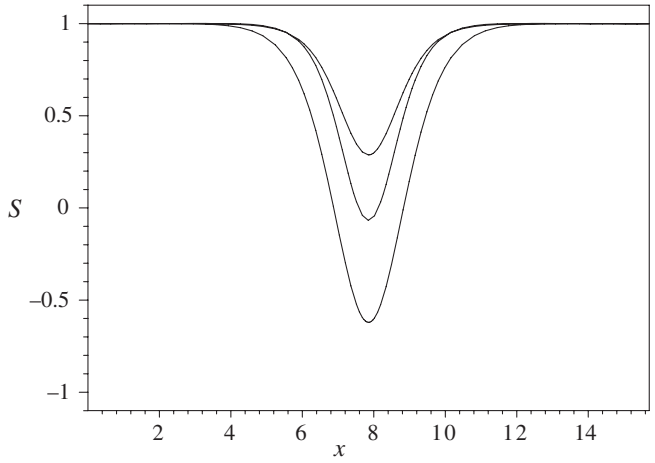

FIG. 1. Self-consistent scalar HF potential $S(x)$ at $T = 0$, $p_f = 0.2$ and $\gamma = 0.2$, 0.6, 1.0 (from bottom to top), showing well-resolved baryons. Here and in Figs. 2–4 only one spatial period of the periodic potentials is shown.

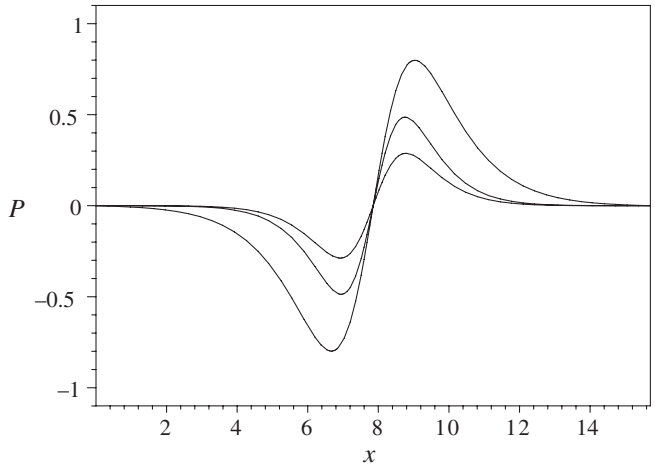

FIG. 2. One period of self-consistent pseudoscalar HF potential $P(x)$ at $T = 0$, $p_f = 0.2$ and $\gamma = 0.2$, 0.6, 1.0 (with decreasing amplitude).

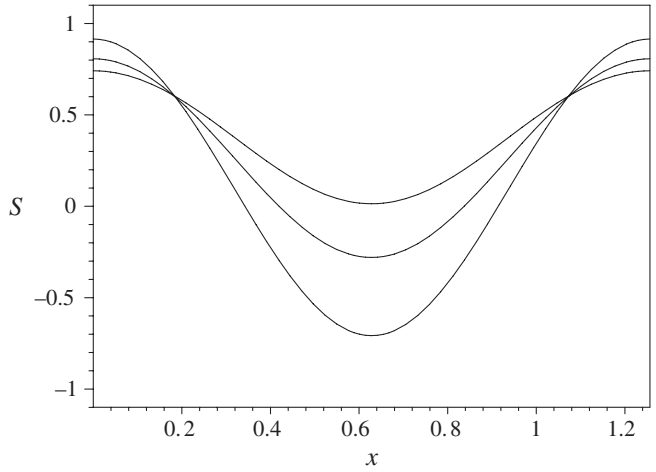

FIG. 3. Same as Fig. 1, but at $p_f = 2.5$ where the baryons overlap strongly.

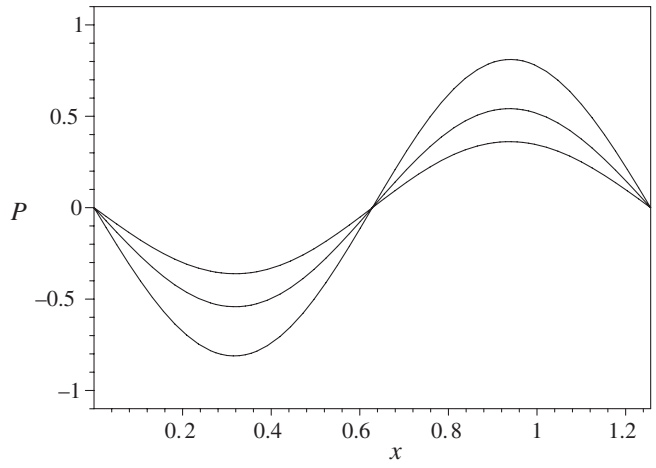

FIG. 4. Same as Fig. 2, but at $p_f = 2.5$.

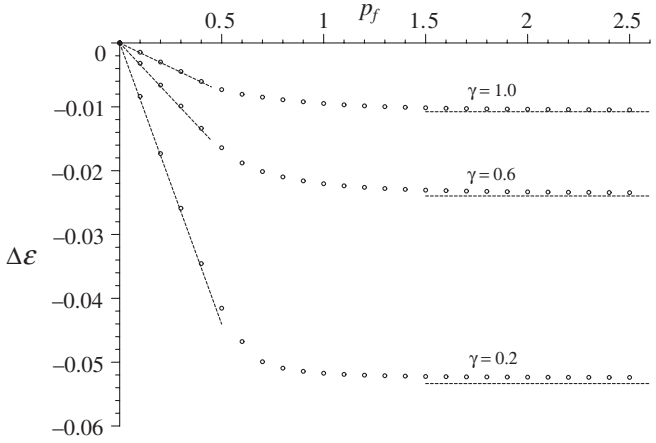

FIG. 5. Difference between energy density of solitonic crystal phase and homogeneous phase versus p_f for 3 different values of γ. The straight line segments drawn show the analytical expectations for small and large p_f, respectively; see the main text.

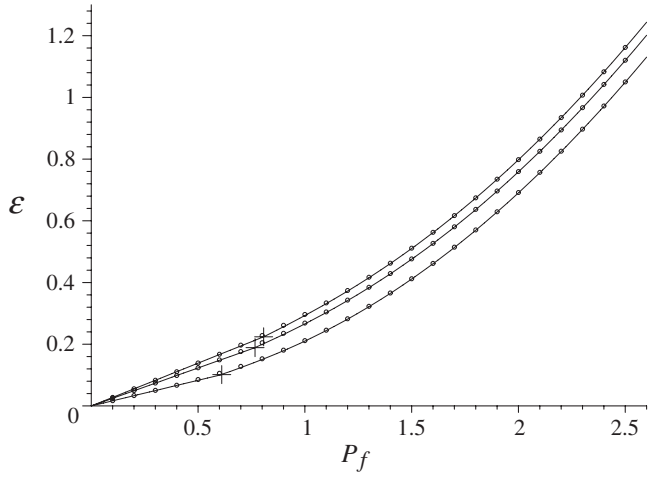

FIG. 6. Ground state energy density of crystal at $T = 0$ as a function of p_f for $\gamma = 0.2, 0.6, 1.0$ from bottom to top. Points represent numerical HF results. Curves represent asymptotic predictions according to Eqs. (13) and (23). They are matched at the point marked by a cross.

cent of similar findings in an earlier numerical study of the nonchiral GN model [20].

III. CONSTRUCTING THE PHASE DIAGRAM

A. Grand canonical potential

The phase diagram in the temperature-chemical potential plane is best analyzed via the grand canonical potential density Ψ. The evaluation of Ψ in the relativistic HF approach is well understood and follows earlier studies of the nonchiral GN model, the only small complication being the fact that the spectrum is no longer symmetric under $E \to -E$. The main building block is the familiar single particle contribution to Ψ,

$$\Psi = -\frac{1}{\beta L}\sum_{\eta,n} \ln(1 + \mathrm{e}^{-\beta(E_{\eta,n}-\mu)}). \tag{24}$$

For large positive or negative energy eigenvalues, one has to use perturbation theory in order to do the renormalization analytically. The corresponding expression is

$$\Psi_{\mathrm{pert}} = -\frac{2}{\beta}\int_{\bar{p}}^{\Lambda/2}\frac{\mathrm{d}p}{2\pi}\sum_{\eta} \ln(1 + \mathrm{e}^{-\beta(E_{\eta,p}-\mu)}) \tag{25}$$

where $E_{\eta,p}$ denotes the 2nd order perturbative eigenvalue of the Dirac-HF Hamiltonian H. The standard manipulation

$$\Psi_{\mathrm{pert}} = -\frac{2}{\beta}\int_{\bar{p}}^{\infty}\frac{\mathrm{d}p}{2\pi}\ln(1 + \mathrm{e}^{-\beta(E_{+1,p}-\mu)}) - \frac{2}{\beta}\int_{\bar{p}}^{\infty}\frac{\mathrm{d}p}{2\pi} \times \ln(1 + \mathrm{e}^{\beta(E_{-1,p}-\mu)}) + 2\int_{\bar{p}}^{\Lambda/2}\frac{\mathrm{d}p}{2\pi}[E_{-1,p} - \mu] \tag{26}$$

isolates the divergence in the sum over single particle energies, which can then be dealt with like at $T = 0$ (see Sec. II and Ref. [17]) adding the double counting correction and using the gap equation to eliminate unphysical parameters. We then minimize Ψ with respect to the potentials S, P. The result is the renormalized grand canonical potential density, together with the self-consistent potential at a given temperature and chemical potential. A vacuum subtraction finally normalizes Ψ to 0 at the point $(T = 0, \mu = 0)$ and removes remaining trivial divergences from the Dirac sea.

B. Ginzburg-Landau theory

There are regions in (γ, μ, T) space where a full HF calculation can be bypassed. This is the case whenever a microscopic GL theory can be derived, leading to an effective bosonic field theory directly in terms of the scalar and pseudoscalar potentials S, P with the fermions ''integrated out''. One can identify two such regions requiring somewhat different approximations. Close to the tricritical point $(\gamma = 0, \mu = 0, T = e^C/\pi)$, the potentials are both weak and slowly varying. This was exploited in Ref. [18], where a GL effective action was obtained analytically, using the derivative expansion around the free, massless fermion theory. The resulting effective action was then minimized by a numerical solution of the Euler-Lagrange equation, an inhomogeneous, complex nonlinear Schrödinger equation. In this manner, a soliton crystal solution could be identified in a small region of (γ, μ, T) space, separated by 2nd and 1st order transitions from a homogeneous massive Fermi gas phase. We refer the reader to this paper for more details. Another approximation allows one to study the phase diagram for $\gamma \ll 1$ and $\mu \ll 1$, but without any restriction in temperature. Here, the potentials are still slowly varying but develop a large, constant scalar term S_0, i.e., a mass. The derivative expansion can still be trusted, provided one expands now around the *massive* free Dirac theory. This technique was applied some time ago at $T = 0$ to the baryons in the chiral GN model near $\gamma = 0$ [16]. The generalization to finite temperature and chemical potential is technically rather involved. In particular, it does not lead anymore to analytic expressions as in Ref. [16], since the thermal integrals with massive single particle energies cannot be done in closed form. As this technique was used here only for a small part of the phase diagram, we refrain from giving all the details which have been worked out in Ref. [21]. The resulting effective action is a polynomial in S, P and its derivatives with (γ, μ, T) dependent coefficients given in terms of one-dimensional numerical integrals. It can be minimized numerically by varying the period and the Fourier coefficients of S and P, resulting in the equilibrium value of Ψ. In this way, it is possible to extend the calculation of the 1st order transition line at small γ down to zero temperature and check that the base point of the critical line coincides with the baryon mass. Some examples of results for the phase boundary thus obtained will be shown below together with the results of the full HF calculation; see Sec. III D and Figs. 11 and 12.

C. Perturbative 2nd order phase boundary

As is well understood by now from similar studies of the nonchiral GN model or from the GL approach near the tricritical point, the exact location of a contingent 2nd order phase boundary between crystal and homogeneous phases is a perturbative matter. For this purpose, S_0 (i.e., the dynamical fermion mass) has to be treated exactly, whereas it is sufficient to keep S_1, P_1 from the inhomogeneous terms and treat them in 2nd order almost degenerate perturbation theory (ADPT). As a matter of fact, right at the phase boundary this amounts to naive 2nd order perturbation theory and a principal value prescription for integrating through the pole when summing over single particle states [20]. The Hamiltonian is divided up according to

$$H = H_0 + V \tag{27}$$

where

$$\begin{aligned} H_0 &= \gamma_5 \frac{1}{\mathrm{i}} \frac{\partial}{\partial x} + \gamma^0 m, \\ V &= \gamma^0 2S_1 \cos(2p_f x) - \mathrm{i}\gamma^1 2P_1 \sin(2p_f x). \end{aligned} \tag{28}$$

To define the notation, we cast the unperturbed problem into the form ($\eta = \pm 1$ is the sign of the energy)

$$H_0|\eta, p\rangle = \eta E|\eta, p\rangle, \qquad E = \sqrt{p^2 + m^2} \tag{29}$$

with the free, massive spinors

$$\langle x|\eta, p\rangle = -\frac{\mathrm{i}\,\mathrm{sgn}(p)}{\sqrt{2LE}} \begin{pmatrix} \mathrm{i}p - m \\ \eta E \end{pmatrix} \mathrm{e}^{\mathrm{i}px}. \tag{30}$$

Matrix elements of V are then given by

$$\langle \eta', p'|V|\eta, p\rangle = \frac{\mathrm{sgn}(p)\mathrm{sgn}(p')}{2EE'} (\mathcal{A}S_1 + \mathcal{B}P_1) \tag{31}$$

with

$$\begin{aligned} \mathcal{A} &= [\eta E(\mathrm{i}p' + m) - \eta' E'(\mathrm{i}p - m)] \\ &\quad \times (\delta_{p',p+2p_f} + \delta_{p',p-2p_f}) \\ \mathcal{B} &= \mathrm{i}[\eta\eta' EE' + (\mathrm{i}p - m)(\mathrm{i}p' + m)] \\ &\quad \times (\delta_{p',p+2p_f} - \delta_{p',p-2p_f}), \end{aligned} \tag{32}$$

leading to the following 2nd order energy shift:

$$\delta E_{\eta,p} = \frac{\eta(E^2 S_1^2 + p^2 P_1^2) + 2p_f E S_1 P_1}{(p^2 - p_f^2)E}. \tag{33}$$

We insert

$$E_{\eta,p} = \eta E + \delta E_{\eta,p} \tag{34}$$

into the single particle contribution to the grand canonical potential density,

$$\Psi = -\frac{2}{\beta}\int_0^{\Lambda/2}\frac{\mathrm{d}p}{2\pi}\ln[(1+\mathrm{e}^{-\beta(E_{1,p}-\mu)}) \times (1+\mathrm{e}^{-\beta(E_{-1,p}-\mu)})], \tag{35}$$

and linearize in $\delta E_{\eta,p}$. Adding the usual HF double counting correction term and invoking the gap equation for the fermion mass at finite T, μ in the translationally invariant case,

$$0 = m(\gamma+\ln m) - \gamma + m\int_0^\infty \frac{\mathrm{d}p}{E}\left(\frac{1}{\mathrm{e}^{\beta(E-\mu)}+1} + \frac{1}{\mathrm{e}^{\beta(E+\mu)}+1}\right), \tag{36}$$

to simplify the resulting expression, the perturbative correction to the grand canonical potential becomes

$$\delta\Psi = \frac{E_f^2 S_1^2 + p_f^2 P_1^2}{\pi}\int_0^\infty \mathrm{d}p\,\frac{1}{E(p^2-p_f^2)}\left(\frac{1}{\mathrm{e}^{\beta(E-\mu)}+1} + \frac{1}{\mathrm{e}^{\beta(E+\mu)}+1}\right) + \frac{2p_f S_1 P_1}{\pi}\int_0^\infty \mathrm{d}p\,\frac{1}{p^2-p_f^2} \times\left(\frac{1}{\mathrm{e}^{\beta(E-\mu)}+1} - \frac{1}{\mathrm{e}^{\beta(E+\mu)}+1}\right) + \frac{S_1^2+P_1^2}{\pi}\frac{\gamma}{m} - \frac{E_f^2 S_1^2 + p_f^2 P_1^2}{2\pi p_f E_f}\ln\left(\frac{E_f - p_f}{E_f + p_f}\right). \tag{37}$$

The energies E, E_f are defined with the mass $m = S_0$ and momenta p, p_f, respectively. The principal value integrals are the only remnant of ADPT at the phase boundary [20] and have to be evaluated numerically. The phase boundary can now be found using the following strategy. In 2nd order perturbation theory, according to Eq. (37) we may write the grand canonical potential schematically as

$$\Psi = \Psi_{\mathrm{hom}} + \mathcal{M}_{11}S_1^2 + 2\mathcal{M}_{12}S_1P_1 + \mathcal{M}_{22}P_1^2 \tag{38}$$

where all coefficients depend on m and p_f. We have to vary Ψ with respect to the 4 parameters, m, S_1, P_1 and p_f. This yields the 4 equations:

$$0 = \frac{\partial\Psi_{\mathrm{hom}}}{\partial m} + S_1^2\frac{\partial\mathcal{M}_{11}}{\partial m} + 2S_1P_1\frac{\partial\mathcal{M}_{12}}{\partial m} + P_1^2\frac{\partial\mathcal{M}_{22}}{\partial m}, \tag{39}$$

$$0 = S_1\mathcal{M}_{11} + P_1\mathcal{M}_{12}, \tag{40}$$

$$0 = S_1\mathcal{M}_{12} + P_1\mathcal{M}_{22}, \tag{41}$$

$$0 = S_1^2\frac{\partial\mathcal{M}_{11}}{\partial p_f} + 2S_1P_1\frac{\partial\mathcal{M}_{12}}{\partial p_f} + P_1^2\frac{\partial\mathcal{M}_{22}}{\partial p_f}. \tag{42}$$

At the phase boundary, Eq. (39) can be simplified to the standard equation for the homogeneous phase since S_1, P_1 vanish,

$$\frac{\partial\Psi_{\mathrm{hom}}}{\partial m} = 0. \tag{43}$$

Equations (40) and (41) represent a homogeneous system of equations which can be cast into the equivalent form

$$\det\mathcal{M} = \mathcal{M}_{11}\mathcal{M}_{22} - \mathcal{M}_{12}^2 = 0, \tag{44}$$

$$\frac{S_1}{P_1} = -\frac{\mathcal{M}_{12}}{\mathcal{M}_{11}}. \tag{45}$$

Dividing Eq. (42) by P_1^2 and using Eqs. (44) and (45), we finally obtain the condition

$$\frac{\partial\det\mathcal{M}}{\partial p_f} = 0. \tag{46}$$

In order to determine the phase boundary, we have to find the points in the (μ, T) plane where Eqs. (43), (44), and (46) hold simultaneously. Equation (45) then yields the unstable direction. All of this can be done numerically to any desired accuracy. Before turning to the results, it may be worthwhile to ask whether we can say anything about the outcome of the calculation beforehand. Indeed, it is easy to determine the asymptotic behavior of the perturbative 2nd order sheet in the limit $\mu\to\infty$, for any γ. Along the lines of a similar analysis in the appendix of Ref. [20] we arrive at the approximate expression for the grand canonical potential valid at large $\mu \approx p_f$,

$$\Psi = \frac{S_0^2}{2\pi}[\gamma+\ln(2p_f)] - \frac{\gamma S_0}{\pi} + \frac{2X^2}{\pi}[\gamma+\ln(4p_f)] + \frac{y^2}{4\pi} \times(2\gamma - 1 + \ln y^2) - \frac{2}{\beta\pi}\int_0^\infty \mathrm{d}p\,\ln(1+\mathrm{e}^{-\beta\sqrt{p^2+y^2}}) \tag{47}$$

(using once again variables $X = (S_1+P_1)/2$, $y = S_1 - P_1$). S_0 and X are not affected by finite temperature at all, so that Eqs. (18) still hold. Minimization with respect to y yields either $y = 0$ (translationally invariant solution) or the condition

$$\gamma + \ln y + 2\int_0^\infty \mathrm{d}p\,\frac{1}{\sqrt{p^2+y^2}}\frac{1}{\mathrm{e}^{\beta\sqrt{p^2+y^2}}+1} = 0. \tag{48}$$

In order to compute the phase boundary, we expand the integral for small y [22],

$$\gamma + \ln y - \ln\frac{\beta y}{\pi} - \mathrm{C} + \mathrm{O}(y^2) = 0, \tag{49}$$

where C is the Euler constant. The critical line where the nontrivial solution for y disappears is then given by the following asymptotic expression valid at large μ:

$$T_{\mathrm{crit}} = \mathrm{e}^{-\gamma}\left(\frac{\mathrm{e}^{\mathrm{C}}}{\pi}\right). \tag{50}$$

Figure 7 shows the results for the perturbative 2nd order sheet (a preliminary version of this plot has been given before in [23]). This figure actually contains the 2nd order sheets for both the chiral and the nonchiral GN models to highlight the differences between the two models. The lower sheet ending at the fat black tricritical line belongs to the GN model with discrete chiral symmetry. To test our method, we have recalculated the curves shown here perturbatively. They agree indeed with the results of Ref. [24] where the same critical surface was deduced from the full, analytical solution of the HF problem. The upper sheet in Fig. 7 is the new result for the chiral GN model. Here we have supplemented the equidistant curves at $\gamma = 0.1, 0.2, \ldots 2.0$ by 2 more curves at the small γ values 0.01 and 0.0001. This is useful to illustrate how this 2nd order sheet goes over into the horizontal critical line $T = e^C/\pi$ in the chiral limit $\gamma \to 0$. We also compare the 2nd order sheet with the analytical prediction, Eq. (50), at large μ. As the dashed curve shows, the full results are already indistinguishable from this formula at $\mu = 2$. At low μ, the curves bend over. Our calculation gives us no clue as to where the tricritical points are beyond which these curves turn into 1st order critical lines. We will get back to this issue in the following subsection when we discuss the full HF calculation. Notice also that at large γ, the perturbative sheets of both variants of the GN model seem to come together at the same line (the tricritical line of the discrete chiral GN model), whereas this does not hold anymore at small γ.

Finally, we should stress the fact that the sheet in Fig. 7 represents the surface where the homogeneous phase becomes unstable towards crystallization in a continuous transition. If a 1st order transition occurs before reaching this sheet from the outside, there will be no 2nd order transition and the corresponding part of the 2nd order sheet becomes obsolete. As shown below, this is indeed what happens at sufficiently low temperatures.

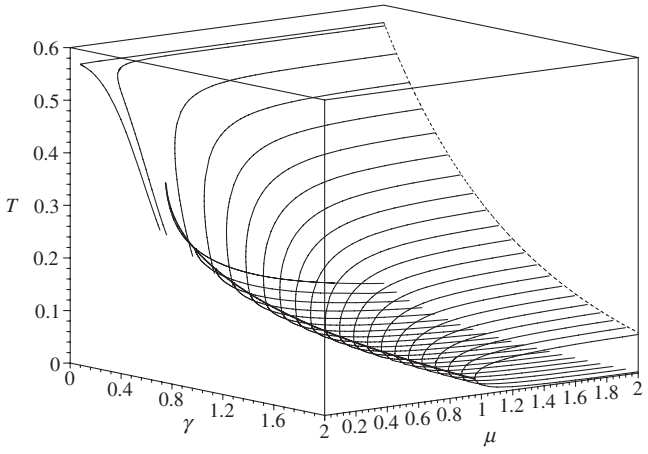

FIG. 7. 3D plot of the perturbative, 2nd order phase boundary in the chiral GN model (upper sheet), compared to the corresponding phase boundary in the nonchiral GN model (lower sheet). The fat line is the tricritical curve of the latter model. The tricritical curve of the chiral GN model cannot be determined by this calculation. The dashed curve at $\mu = 2$ is the asymptotic prediction of Eq. (50).

D. Nonperturbative 1st order phase boundary and full phase diagram

The most tedious task of the present study is to determine the 1st order phase boundary. For arbitrary γ and μ, no shortcut like GL theory is known and we have to resort to the full, numerical HF calculation. For a given point in the (γ, μ, T) diagram, we evaluate the renormalized grand canonical potential density Ψ by minimization with respect to the period a and the Fourier components S_ℓ, P_ℓ of the mean field. The critical line is then constructed as follows. We evaluate Ψ along a straight line trajectory for fixed γ, T and several equidistant values of μ, starting from inside the anticipated crystal phase and proceeding towards lower μ values. We then plot Ψ against μ and compare this thermodynamic potential with the one of the homogeneous solution. In Fig. 8, we illustrate the outcome of such a computation for the case $\gamma = 1.0$, $T = 0.08$. The thermodynamically stable phase is the one with the lowest value of Ψ, hence the point of intersection of the 2 curves defines the critical chemical potential at this temperature. Since we can follow the crystal solution beyond this point (before it jumps onto the other curve), this is clearly a 1st order transition where two different solutions coexist at the phase boundary. The difference in slopes at the intersection point translates into two different densities, so that a mixed phase would appear in a (ρ, T) phase diagram. The critical point can be determined accurately in cases like that shown in Fig. 8. By contrast, Fig. 9 illustrates an example where

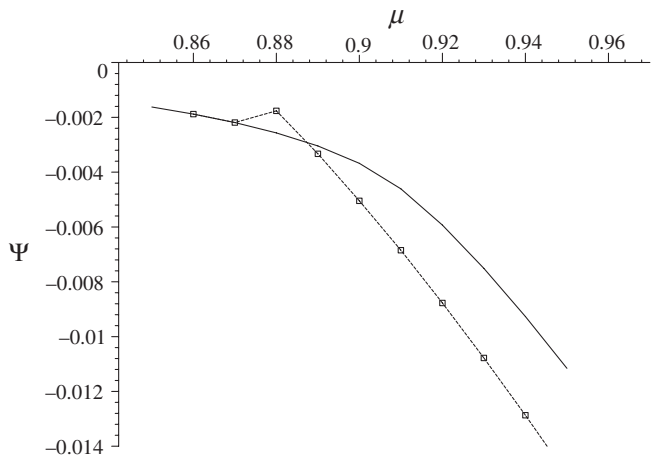

FIG. 8. Determination of the 1st order phase boundary at $T = 0.08$, $\gamma = 1.0$. Points: Grand canonical potential from numerical HF calculation vs μ. The crystal phase can be followed down to $\mu = 0.88$. Solid line: Prediction assuming homogeneous condensates only. The crossing of the 2 lines yields the critical chemical potential for a 1st order transition.

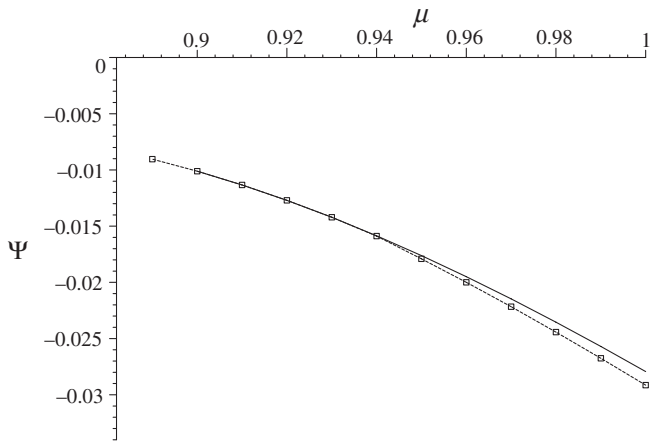

FIG. 9. Same plot as in Fig. 8 at $T = 0.12$, $\gamma = 1.0$. The absence of line crossing is indicative of a continuous, 2nd order phase transition.

the transition is likely to be 2nd order, namely, at $\gamma = 1.0$, $T = 0.12$. Here, one does not see a crossing of the two curves. Because of the limited numerical accuracy, one cannot rule out a very weak first order transition, therefore it is difficult to locate the tricritical point precisely in this manner.

The result of such a computation of the 1st order critical line at $\gamma = 1.0$ is shown in Fig. 10. The solid line is the perturbative 2nd order line from Sec. II C and Fig. 7, without information on the tricritical point. The squares are numerically determined 1st order phase transitions. We only show those points for which we could unambiguously identify a 1st order transition. Above $T = 0.1$, there was no visible line crossing anymore. In this way, a small gap between the 2nd and 1st order phase boundaries is left. All

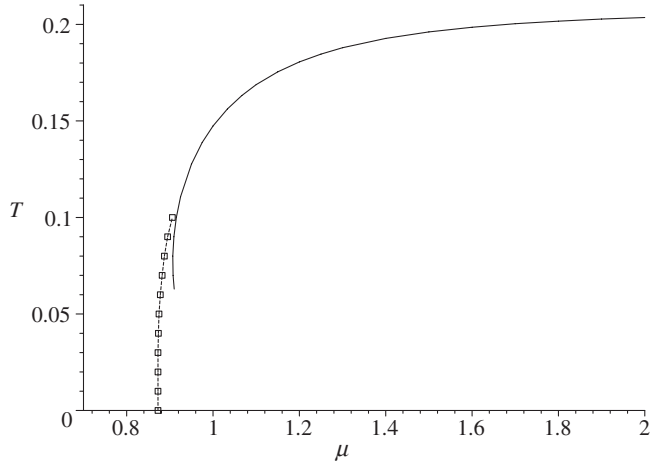

FIG. 10. Example of a construction of the phase boundaries at $\gamma = 1.0$. Solid line: 2nd order, perturbative critical line from Fig. 7. Points: 1st order, nonperturbative critical line determined as shown in Fig. 8. The tricritical point has not yet been located but must lie on the solid line, above $T = 0.1$.

we can say is that the tricritical point lies on the 2nd order line above the last 1st order point shown, i.e., at $T > 0.10$ in the case at hand. For as much as we can tell, the two critical lines are joined tangentially at the tricritical point. Note that the base point of the 1st order line at $T = 0$ drawn here is the baryon mass at $\gamma = 1.0$ taken from Ref. [17]. The fact that the numerical points interpolate nicely between the baryon mass at $T = 0$ and the perturbative phase boundary is a healthy sign, suggesting that the accuracy reached here is adequate.

In a lengthy numerical calculation with MAPLE, we have determined a number of 1st order critical lines, see Fig. 11. The solid curve at $T = 0$ is the baryon mass from Ref. [17]. The thin lines are the 2nd order critical lines from Fig. 7, the points are numerically determined 1st order transitions computed on a grid with resolution $\Delta\gamma = 0.1$, $\Delta T = 0.01$. Also shown are two additional curves at very small γ (0.01 and 0.0001) obtained previously by means of the GL theory [21]. These results confirm the picture discussed in connection with Fig. 10 and provide us with a first candidate for the full phase diagram of the chiral GN model. We find no indication of any further phase transitions beyond those which have been identified in the earlier study near the tricritical point [18].

In Fig. 11, we have also plotted a tricritical line where the 1st and 2nd order critical sheets are joined together. As is clear from the gap between the calculated 1st order sheet and this line, some extrapolation had to be used. We proceeded as follows. For a fixed value of γ, we move along the 2nd order instability line, starting well below the expected tricritical point. We then perform the HF minimization and follow, in particular, the evolution of the

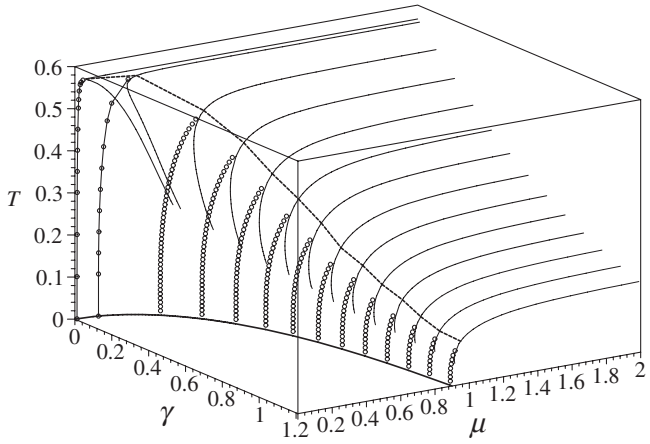

FIG. 11. Summary of all the results about the phase diagram of the chiral GN model obtained in this work. Fat solid curve at $T = 0$: Baryon mass. Solid lines at fixed γ: Perturbative 2nd order sheet. Points: numerically determined 1st order sheet, computed in steps of $\Delta\gamma = 0.1$, $\Delta T = 0.01$. The 2 curves at very small γ are taken from the GL analysis [21] and belong to $\gamma = 0.01$ and 0.0001, respectively. The fat line crossing the 2nd order sheet is the tricritical curve.

largest Fourier components S_1, P_1. At the tricritical point, these are expected to vanish with some power law $\sim(T_c - T)^{\alpha}$. In order to find the relevant critical exponent α, we went back to the GL approach near $\gamma = 0$ [18] and performed a similar analysis there. This has the advantage that we can work with a much higher numerical precision in this regime. Let us first recall that to take advantage of simple scaling properties near the tricritical point, the variables μ, T have been replaced by the rescaled variables

$$\nu = 2\gamma^{-1/3}\mu, \qquad \sigma = \sqrt{\frac{a}{T_c}}\gamma^{-1/3}\sqrt{T_c - T} \tag{51}$$

with $a = 6.032$, $T_c = 0.5669$ in Ref. [18]. We now move along the perturbative phase boundary plotted in Fig. 6 of [18] between $\sigma = 1.4$ and 1.6 enclosing the tricritical point. Along this trajectory the effective action is minimized with respect to the Fourier components of S_ℓ, P_ℓ ($\ell \leq 4$) and the period. The resulting grand canonical potential is compared to the homogeneous calculation in Fig. 12. Figure 13 then shows clearly that the Fourier components S_1, P_1 vanish like $\sigma^{1/2} \sim (T_c - T)^{1/4}$. (Notice that the grand canonical potential and the Fourier components in Figs. 12 and 13 have been rescaled by the factors $2\pi a/\gamma$ and $\gamma^{-1/3}$, respectively; cf. Ref. [18].) As a by-product, we have determined in this way a more accurate value of the tricritical point near $\gamma = 0$ than in Ref. [18], namely $\sigma_t = 1.464$, $\nu_t = 3.039$. Coming back to the full HF calculation, we have located the point where S_1, P_1 vanish along the 2nd order instability curve assuming the same critical exponent $\alpha = 1/4$ for all γ. Because of numerical limitations, the extrapolation is not as quantitative as in Fig. 13, but still fairly straightforward. The result is the tricritical curve drawn in Fig. 11.

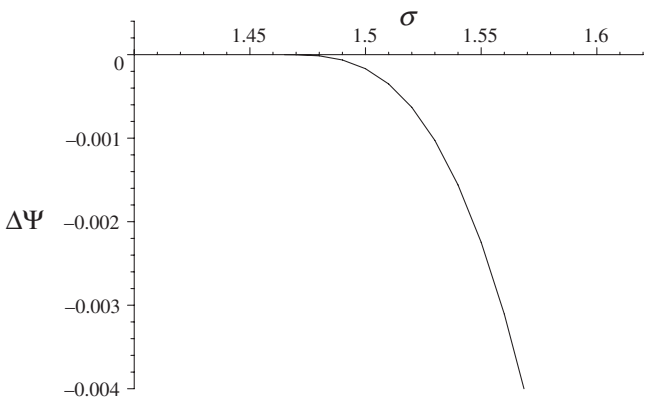

FIG. 12. Difference in grand canonical potential between 2 phases near the tricritical point, using GL theory near $\gamma = 0$. The rescaled potential difference is plotted vs $\sigma \sim (T_c - T)^{1/2}$ along the 2nd order critical line.

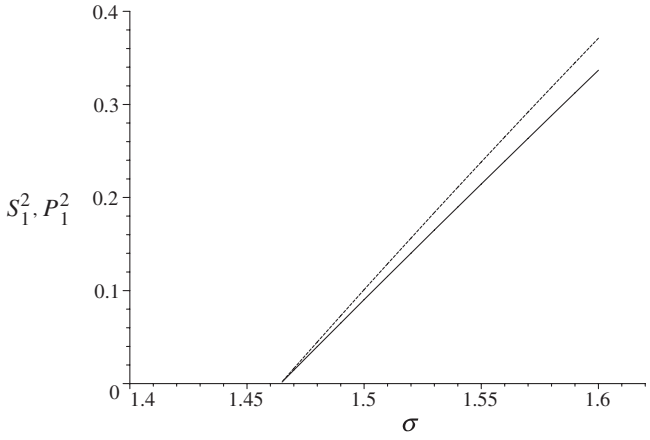

FIG. 13. Square of rescaled Fourier amplitudes S_1 (solid line) and P_1 (dashed line) vs σ for the calculation corresponding to Fig. 12. The linear behavior shows that $S_1, P_1 \sim (T_c - T)^{1/4}$ and locates the tricritical point precisely at $\sigma = 1.464$.

IV. SUMMARY AND CONCLUSIONS

To summarize, we have redrawn the phase diagram of Fig. 11 in a way which shows more clearly the shape of the 2 critical sheets, see Fig. 14. Here, we hide the "engineering details" of the underlying construction still visible in Fig. 11. Whereas the vertical (1st order) lines have actually been computed via HF, the horizontal lines are composed of straight line segments joining neighboring points to guide the eye. The tricritical line separates 1st and 2nd order sheets. It is not completely smooth since this particular curve is the most difficult part of the whole calculation, exceptionally sensitive to numerical inaccuracies.

It is interesting to compare this newly determined phase diagram of the massive chiral GN model to other related phase diagrams. For this purpose, we have taken the results for the discrete chiral GN model from Ref. [24] and plotted

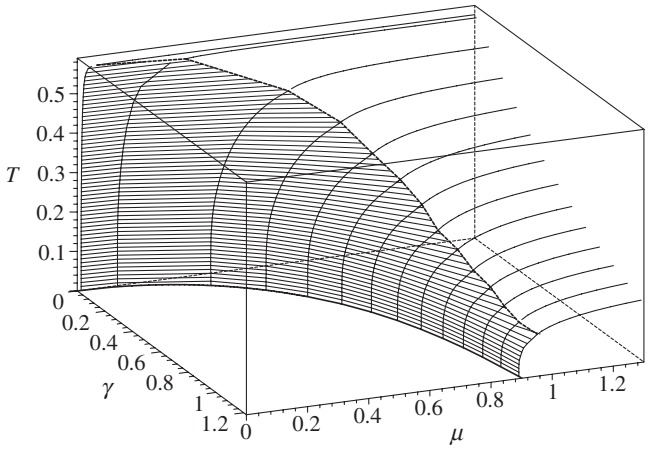

FIG. 14. Phase diagram of the massive chiral GN model. The crystal phase with complex order parameter is separated from the massive Fermi gas phase by 1st (dark shaded) and 2nd (light shaded) order critical sheets joined at a tricritical line.

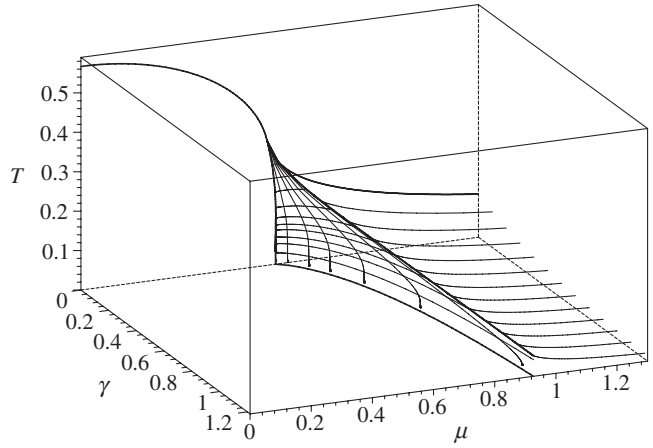

FIG. 15. Phase diagram of the massive discrete chiral GN model, adapted from Ref. [24]. The crystal phase with real order parameter is separated by two 2nd order critical sheets from the massive Fermi gas phase, meeting at the tricritical line.

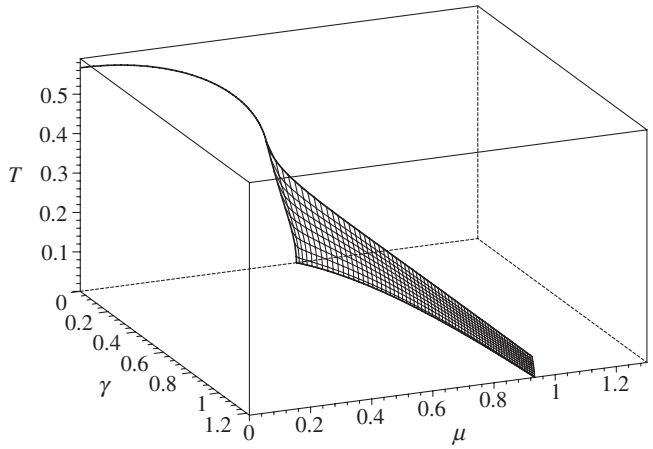

FIG. 16. Common phase diagram for both variants of the massive GN model, assuming homogeneous condensates only. There is only a single massive Fermi gas phase, but the value of the mass changes discontinuously across the dark shaded 1st order sheet. The tricritical line agrees with the one in Fig. 15. Adapted from Refs. [14,24].

them at the same scale and under the same viewing angle as in Fig. 14; cf. Fig. 15. Here the 2 critical sheets are both 2nd order and joined in a cusp rather than tangentially. The qualitative differences between Figs. 14 and 15 are due to the difference between continuous and discrete chiral symmetries of the two GN-type models, reflecting the corresponding universality classes. If one would only admit homogeneous phases as was done in the early works on these phase diagrams, the 2 models would give identical results. This is illustrated in Fig. 16 adapted from Ref. [24]. Here, the dark shaded sheet is 1st order, and there is only a single massive Fermi gas phase at $\gamma > 0$.

Let us finally comment on some open questions. As pointed out above, to determine the tricritical line of the chiral GN model requires some extrapolation of numerical results. The minimization becomes difficult close to the tricritical line where the effective potential is flat. Independent analytical work on the tricritical line and the critical exponent α discussed above would therefore be useful. One would also like to know the universality classes to which the different variants of GN models belong.

Another issue where further work is needed is related to the possibility of chiral twist in the massless case, recently discovered in Ref. [12]. From the symmetry point of view, the situation in the chiral limit may be characterized as follows: The Hamiltonian commutes with the generators (P, Q, Q_5) of translations and vector/axial vector phase transformations of the fermions. A mass term (like in the vacuum or any homogeneous phase) breaks Q_5, reducing chiral symmetry to U(1) vector transformations with the appearance of a massless Goldstone boson, the pion, and leaves P unbroken. The chiral spiral solution breaks P and Q_5, but leaves the linear combination $P + \mu Q_5$ unbroken. Since one unbroken, continuous symmetry is left, one expects only one gapless excitation, a mixture of a phonon and a pion. If the twisted kink crystal is realized, the symmetry will be further broken down to one discrete combination of translation and γ_5 phase rotation; cf. Eq. (11). Such crystals should feature two different gapless excitations, the phonon and the pion. In view of these different physics implications, it is important to reconsider the phase diagram in the chiral limit once again and establish the thermodynamically most stable phases.

In the massive chiral GN model, chiral symmetry is explicitly broken by the bare mass term, and Q_5 does not commute with H anymore. It is therefore unlikely that the Q_5 operator appears in a residual discrete symmetry of the condensates, as in the chirally twisted kink crystal. The only remaining issue is then the fate of translational symmetry and its generator P. So far, we have tacitly assumed that translational invariance breaks down to a discrete subgroup with concomitant periodic potentials, as is common in condensed matter systems. If this assumption would turn out to be wrong, the present calculation should be regarded as a variational calculation rather than the exact solution of the model in the large N limit, but such a scenario does not seem very likely to us.

ACKNOWLEDGMENTS

One of the authors (M. T.) wishes to thank Gerald Dunne for helpful comments and discussions.

[1] G. 't Hooft, Nucl. Phys. **B75**, 461 (1974).
[2] D. J. Gross and A. Neveu, Phys. Rev. D **10**, 3235 (1974).
[3] V. Schön and M. Thies, *At the Frontier of Particle Physics: Handbook of QCD, Boris Ioffe Festschrift*, edited by M. Shifman (World Scientific, Singapore, 2001), ch. 33, p. 1945, vol. 3.
[4] M. Thies, J. Phys. A **39**, 12707 (2006).
[5] G. Basar and G. V. Dunne, arXiv:0806.2659 [Phys. Rev. D (to be published)].
[6] Y. Nambu and G. Jona-Lasinio, Phys. Rev. **122**, 345 (1961); **124**, 246 (1961).
[7] R. F. Dashen, B. Hasslacher, and A. Neveu, Phys. Rev. D **12**, 2443 (1975).
[8] U. Wolff, Phys. Lett. **157B**, 303 (1985).
[9] R. E. Peierls, *Quantum Theory of Solids* (Clarendon, Oxford, 1955), p. 108.
[10] V. Schön and M. Thies, Phys. Rev. D **62**, 096002 (2000).
[11] J. L. Davis, M. Gutperle, P. Kraus, and I. Sachs, J. High Energy Phys. 10 (2007) 049.
[12] G. Basar and G. V. Dunne, Phys. Rev. Lett. **100**, 200404 (2008).
[13] J. Feinberg and A. Zee, Phys. Lett. B **411**, 134 (1997).
[14] A. Barducci, R. Casalbuoni, M. Modugno, G. Pettini, and R. Gatto, Phys. Rev. D **51**, 3042 (1995).
[15] L. L. Salcedo, S. Levit, and J. W. Negele, Nucl. Phys. **B361**, 585 (1991).
[16] M. Thies and K. Urlichs, Phys. Rev. D **71**, 105008 (2005).
[17] C. Boehmer, F. Karbstein, and M. Thies, Phys. Rev. D **77**, 125031 (2008).
[18] C. Boehmer, M. Thies, and K. Urlichs, Phys. Rev. D **75**, 105017 (2007).
[19] M. Thies and K. Urlichs, Phys. Rev. D **72**, 105008 (2005).
[20] M. Thies and K. Urlichs, Phys. Rev. D **67**, 125015 (2003).
[21] S. Kraus, Diploma thesis, Erlangen, 2007, available at http://theorie3.physik.uni-erlangen.de/theses/Dip-1995-.html (in German).
[22] L. Dolan and R. Jackiw, Phys. Rev. D **9**, 3320 (1974).
[23] U. Fritsch, Diploma thesis, Erlangen, 2007, available at http://theorie3.physik.uni-erlangen.de/theses/Dip-1995-.html (in German).
[24] O. Schnetz, M. Thies, and K. Urlichs, Ann. Phys. (N.Y.) **321**, 2604 (2006).